ARTICLE OPEN

Check for updates

Dual topological states in the layered titanium-based oxypnictide superconductor $BaTi_2Sb_2O$

Z. Huang[1,2,3,11], W. L. Liu[1,2,3,11], H. Y. Wang[3,11], Y. L. Su[3,11], Z. T. Liu[1,11], X. B. Shi[4,5], S. Y. Gao[6], Z. Y. Chen[7], Y. J. Yan[7], Z. C. Jiang[1], Z. H. Liu[1,2], J. S. Liu[1], X. L. Lu[1], Y. C. Yang[1], R. X. Zhou[3,8], W. Xia[3,9], Y. B. Huang[10], S. Qiao[1], W. W. Zhao[4,5], Y. F. Guo[3,9]✉, G. Li[3,9]✉ and D. W. Shen[1,2]✉

Topological superconductors have long been predicted to host Majorana zero modes which obey non-Abelian statistics and have potential for realizing non-decoherence topological quantum computation. However, material realization of topological superconductors is still a challenge in condensed matter physics. Utilizing high-resolution angle-resolved photoemission spectroscopy and first-principles calculations, we predict and then unveil the coexistence of topological Dirac semimetal and topological insulator states in the vicinity of Fermi energy (E_F) in the titanium-based oxypnictide superconductor $BaTi_2Sb_2O$. Further spin-resolved measurements confirm its spin-helical surface states around E_F, which are topologically protected and give an opportunity for realization of Majorana zero modes and Majorana flat bands in one material. Hosting dual topological states, the intrinsic superconductor $BaTi_2Sb_2O$ is expected to be a promising platform for further investigation of topological superconductivity.

npj Quantum Materials (2022)7:70; https://doi.org/10.1038/s41535-022-00477-z

INTRODUCTION

Topological superconductors have attracted tremendous interest for harboring Majorana bound states (MBSs) on their boundaries[1–13]. The non-Abelian Majorana zero modes in the vortex of topological superconductors are potential for topological quantum computations without decoherence[14–16]. To date, several systems have been predicted to host topological superconductivity (TSC). Two routes include intrinsic odd-parity superconductors[17–20] and those heterostructures constructed by proximity coupling of topological insulators (TIs)[21,22] or Rashba semiconductors[4,9,23–30] to conventional *s*-wave superconductors, which inspired enormous experimental efforts to the exploration of Majorana fermions[31–63]. However, pairing symmetries of several proposed intrinsic *p*-wave superconductors are yet inconclusive. Meanwhile, difficulties in fabricating heterostructures based on proximity effect and the disturbance of interface physics would inevitably prohibit their further studies.

The recent discovery of MBSs in the iron-based superconductor, combining nontrivial topological states and superconductivity in a single material, pointed out a new dimension in realizing TSC[64–71]. One later research on Li(Fe,Co)As revealed that iron-based superconductors might generically host multiple types of nontrivial topological states, e.g., both the TI and topological Dirac semimetal (TDS), together with unconventional superconductivity[72]. Thus, the surface states of these topological states near the Fermi level (E_F) would participate in the superconducting pairing, hence the possible existence of multiple types MBSs. However, the Dirac point (DP) from the TDS states of superconducting Li(Fe,Co)As with 3% Co is located above the E_F, and thus the proposed one-dimensional Majorana fermion would not be expected to dominate the low-energy electronic structure[72]. Furthermore, seemingly the superconductivity would be inexorably suppressed by introducing further charge carriers in Li(Fe,Co)As[73,74]. In this regard, it is critical to search for more practical superconductors with both surface Dirac cones from TI and TDS states below E_F to realize multiple MBSs in one material.

In this work, we have identified both TI and bulk DP states reminiscent of those in iron-based superconductors but with Dirac cones below E_F in superconducting $BaTi_2Sb_2O$ samples using angle-resolved photoemission spectroscopy (ARPES) and first-principles calculations. Moreover, spin-resolved ARPES measurements confirmed both of the predicted spin-helical surface TI bands and TDS bands, which are prospective to harbour Majorana zero modes and Majorana flat bands in one single material when the superconducting gap open as probed in our scanning tunneling microscopy (STM) measurement. This titanium-based oxypnictide superconductor which has the similar multiple topological states as iron-based superconductors would provide another parallel but more practical playground for comparative study on TSC.

RESULTS

The crystal structure and calculated band structure

The crystal structure of $BaTi_2Sb_2O$ is illustrated in Fig. 1(a). It is composed of $[Ti_2Sb_2O]^{2+}$ octahedron layers, which are stacked with Ba atoms along the *c* axis. Thus, the natural cleavage plane

[1]Center for Excellence in Superconducting Electronics, State Key Laboratory of Functional Materials for Informatics, Shanghai Institute of Microsystem and Information Technology, Chinese Academy of Sciences, Shanghai 200050, China. [2]Center of Materials Science and Optoelectronics Engineering, University of Chinese Academy of Sciences, 100049 Beijing, China. [3]School of Physical Science and Technology, ShanghaiTech University, Shanghai 201210, China. [4]State Key Laboratory of Advanced Welding and Joining, Harbin Institute of Technology, Shenzhen 518055, China. [5]Flexible Printed Electronics Technology Center, Harbin Institute of Technology, Shenzhen 518055, China. [6]Beijing National Laboratory for Condensed Matter Physics and Institute of Physics, Chinese Academy of Sciences, 100190 Beijing, China. [7]Hefei National Laboratory for Physical Sciences at the Microscale, and Department of Physics, University of Science and Technology of China, Hefei 230026, China. [8]Institute for Advanced Study, Tsinghua University, 100084 Beijing, China. [9]ShanghaiTech Laboratory for Topological Physics, ShanghaiTech University, Shanghai 201210, China. [10]Shanghai Synchrotron Radiation Facility, Shanghai Advanced Research Institute, Chinese Academy of Sciences, 201204 Shanghai, China. [11]These authors contributed equally: Z. Huang, W. L. Liu, H. Y. Wang, Y. L. Su, Z. T. Liu. ✉email: guoyf@shanghaitech.edu.cn; ligang@shanghaitech.edu.cn; dwshen@mail.sim.ac.cn

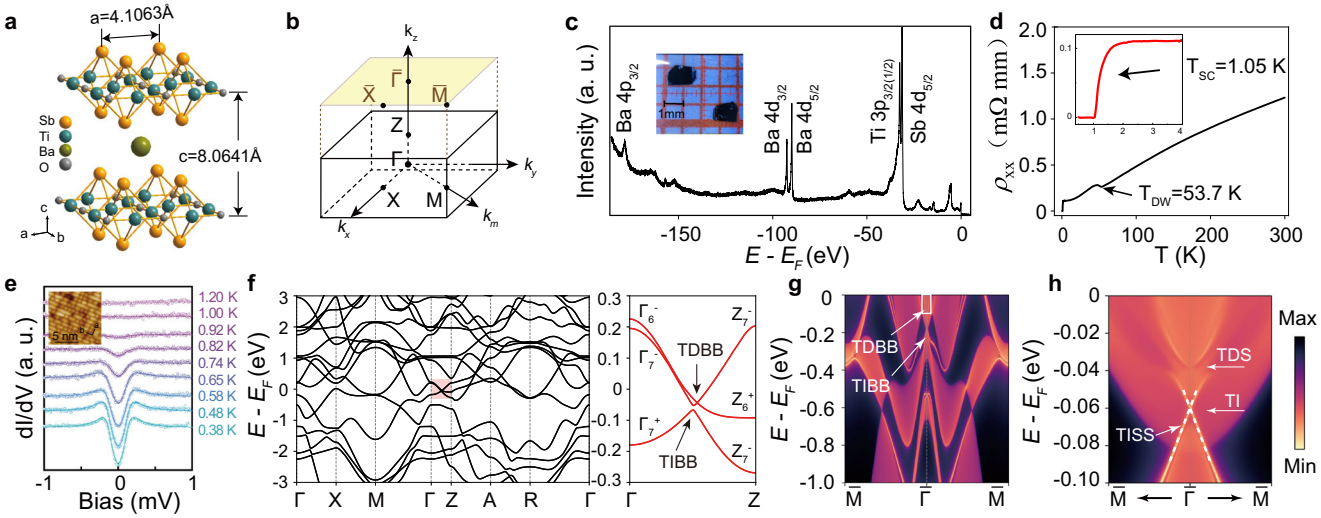

Fig. 1 Crystal structure and calculated band structure. a Crystal structure of layered $BaTi_2Sb_2O$. **b** Three dimensional bulk Brillouin zones (black) with (001) surface Brillouin zone (yellow) projected. High symmetry points are marked. **c** Core-level photoemission spectrum shows strong characteristic Ba, Ti and Sb peaks. Inset: Image of high quality $BaTi_2Sb_2O$ single crystal. **d** Temperature-dependence of resistivity of $BaTi_2Sb_2O$. **e** The evolution of the STS spectra measured at temperatures from 0.38 to 1.20 K with Dynes function fitting results. Measurement condition: $V_b = 1$ mV, I =100 pA, $\Delta V = 20$ μV. Inset: STM topographic image of the in-situ cleaved (001) surface of $BaTi_2Sb_2O$ measured at 0.4 K. Measurement condition: 10 nm × 10 nm, $V_b = 100$ mV, I = 45 pA. **f** Calculated band structure with SOC. The enlarged image of the red region announces the TDS and TI states. **g** Calculated band dispersions along $\bar{\Gamma}$-$\bar{M}$ direction with bulk bands TDBB and TIBB marked. **h** Zoom-in of the white box in (**g**) with surface bands TDSS and bulk DP marked.

should be parallel to the *a*-*b* plane and between two neighbouring $[Ti_2Sb_2O]^{2+}$ layers[75]. The bulk and (001)-projected surface Brillouin zones (BZs) of $BaTi_2Sb_2O$ are shown in Fig. 1(b). Figure 1(c) displays the angle-integrated photoemission spectrum of $BaTi_2Sb_2O$ over a large range of binding energy, in which we can clearly identify the Ba (*4p* and *4d*), Ti (*3p*) and Sb (*4d*) core levels, confirming the element composition of our samples. After cleaved in the air, the sample shows typical flat and shining surface as illustrated in the inset of Fig. 1(c). The sample exhibits a metallic temperature dependence and shows zero resistance below $T_c = 1.05$ K [the inset of Fig. 1(d)]. Temperature-dependent STS data of $BaTi_2Sb_2O$ in Fig. 1(e) shows pronounced superconducting gap which is clearly visible at the lowest accessible temperature, T = 0.38 K. With increasing temperature the gap size is reduced and vanishes at about T ~ 1.0 K. The inset of Fig. 1(e) shows an atomically resolved topographic image of the cleaved $BaTi_2Sb_2O$ single crystal exhibiting homogeneous features. The cleavage plane is expected to be the Ba-termination same as that in ARPES measurements, on which there forms a 2×1 reconstruction since about half of the Ba atoms are lost during the cleavage leaving one half of Ba atoms on another surface[76]. More details on the sample characterizations can be found in Supplementary Note 1.

Figure 1 (f) declares the calculated band structure of $BaTi_2Sb_2O$ with the SOC. We concentrate on crossings of several bands around E_F, which are highlighted by the enlarged image in the right panel. These three bands belong to irreducible representations Γ_6^-, Γ_7^-, and Γ_7^+, respectively. From top to bottom, the three bands between $\Gamma - Z$ connect in the following way: 1. $\Gamma_6^- \rightarrow Z_6^+$, 2. $\Gamma_7^- \rightarrow Z_7^-$, and 3. $\Gamma_7^+ \rightarrow Z_7^-$. The crossing of the 1st and the 3rd bands at an arbitrary k_z along Γ-*Z* features a symmetry-protected DP with parity inversion. Slightly lower in energy, the 2nd and the 3rd bands cross, leading to a small gap. The distinct behavior of these two band crossings stems from different mechanisms. $BaTi_2Sb_2O$ belongs to the space group no. 123, which respects the inversion symmetry $\hat{\mathcal{I}}$. The joint operation of time-reversal ($\hat{\mathcal{T}}$) and $\hat{\mathcal{I}}$ promises the Kramer's double degeneracy everywhere in the BZ. In this case, $\hat{c}_4$, which leaves k_z invariant along Γ-*Z*, protects a stable DP between Γ_6^- and Γ_7^- bands. However, as Γ_7^- and Γ_7^+ share the same basis functions with the only difference on their response to $\hat{\mathcal{I}}$, the two bands will unavoidably open a gap when they cross. Such particular alignment of bands is essential for $BaTi_2Sb_2O$ to resemble the electronic structure of iron-based superconductors which features a great potential to coexist two distinct types of topological superconductivity in one system, i.e., the one-dimensional Majorana fermion from topological DPs and Majorana zero modes from the topological insulator or DPs[72,77]. To better understand the different symmetry-protection and gap opening mechanisms, we present a $k \cdot p$ model for the DP and the gap below with $\hat{c}_4$ and $\hat{\mathcal{T}}\hat{\mathcal{I}}$ in Supplementary Note 2.

The surface states TISS associated with the topological insulating gap and the TDBB states can be further displayed in the surface states calculation along $\bar{\Gamma}$-$\bar{M}$. Here, two bulk bands near $\bar{\Gamma}$ are marked as TDBB and TIBB, respectively [Fig. 1(g)]. By zooming in the region of the white box, we can identify two surface cone-like states, as highlighted by dashed lines in Fig. 1(h). The upper one originates from the hybridization of the bulk DP and other trivial bulk bands, and the lower one should be the TI surface state. Since these two DPs are as close as ~ 23 meV and their overlapped states have gradually merged into bulk states, it is really challenging to distinguish the dispersion between the dual states band gap from photoemission intensity plots. Therefore, we try to resolve the lower part of the surface state from TI, which can be assigned as TISS. We note that these surface states are both below E_F and thus can be probed by ARPES without further carrier doping.

The ARPES results of dual topological bulk bands and related surface states

Experimentally, we first revealed both the TDS and TI bulk states of $BaTi_2Sb_2O$. Due to considerable entanglement between the bulk and surface states around E_F [Fig. 1(g)], we took advantage of the matrix element effect to distinguish between them by using *p*- and *s*-polarized photons[65,78]. The detailed experiment geometry is shown in Supplementary Fig. S2 and Note 3. Figure 2(a) exhibits the photoemisson intensity plot along $\bar{\Gamma}$-$\bar{M}$ with *p*-polarized 100 eV photons, corresponding to the k_z plane nearly intersecting both predicted DPs [see details in Supplementary Note 4]. Figure 2(b)(*i*) and (*ii*) present photoemission intensity map and calculated result

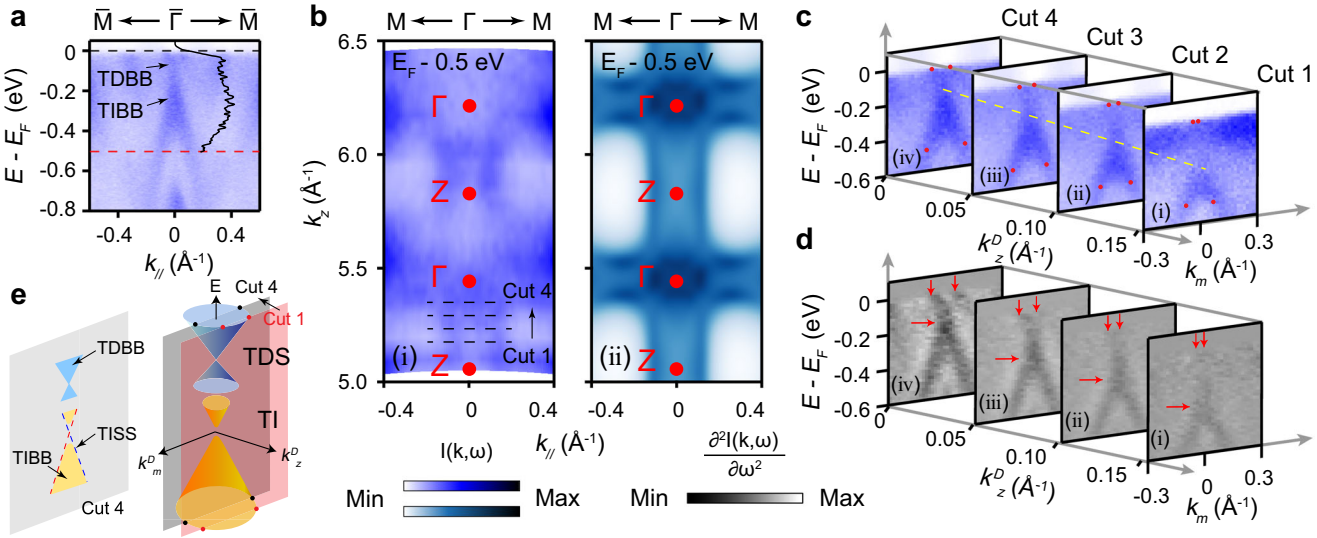

Fig. 2 Dual topological bulk bands. a Intensity plot along $\bar{\Gamma}$-$\bar{M}$ direction with *p*-polarized 100 eV photons. Two bulk band (marked as TDBB and TIBB) near $\bar{\Gamma}$ point are dominated. **b** Intensity plot of k_z dependent ARPES data (i) and corresponding bulk calculated result (ii) along Γ-*M* direction with *p*-polarized photons at E_F - 0.5 eV, which indicate the k_z dispersion of TIBB. **c** ARPES intensity plot along $\bar{\Gamma}$-$\bar{M}$ direction at different k_z indicated by black dashed lines marked as Cut 1 to 4 in (**b**) with $h\nu = 94$, 96, 98 and 100 eV *p*-polarized photons. **d** Second derivative plot of (**c**). **e** Schematic of projected two Dirac cone from TDS and TI into the (k_m, k_z, E) space.

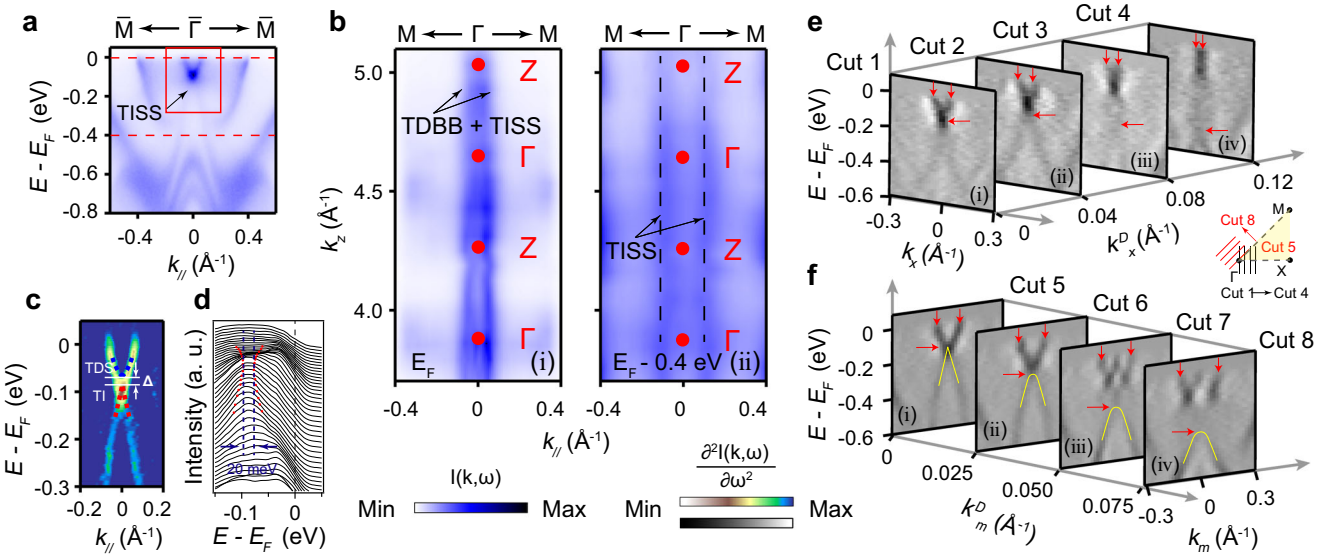

Fig. 3 The topological surface states. a Intensity plot along $\bar{\Gamma}$-$\bar{M}$ direction with *s*-polarized 52 eV photons. The sharp surface states (TISS) near $\bar{\Gamma}$ point are dominated. **b** Intensity plot of k_z dependent ARPES data along Γ-*M* direction with *s*-polarized photons at E_F(***i***) and E_F - 0.4 eV (***ii***), which indicate the k_z dispersion of TDBB hybridizating with TISS and TISS, respectively. **c**, **d** Second derivative plot and EDCs of the region in the red box in (**a**). A gap between two Dirac points is marked. **e**, **f** Second derivative intensity plots taken at $k_x^D = 0$, 0.04, 0.08, 0.12 Å^{-1} and $k_m^D = 0$, 0.025, 0.05, 0.075 Å^{-1}, respectively. Cuts 1 to 8 are illustrated.

on the $k_m - k_z$ plane [the k_m direction is indicated in Fig. 1(b)] taken with *p*-polarized photons at E_F - 0.5 eV, respectively. Band dispersions with apodictic periodic modulation along k_z could be recognized, confirming the bulk nature of TIBB. Furthermore, we show four photoemission intensity plots taken at different k_z as schematically illustrated in Fig. 2(e), from Cut 1 [Fig. 2(c)(*i*)] to Cut 4 [Fig. 2(c)(*iv*)]. The dispersion of TIBB varies from the parabolic lineshape to quasi-linear, and the apex keeps drifting up (highlighted by the yellow dashed line), showing the typical feature of a TI bulk cone [Fig. 2(e)]. In addition, the corresponding second derivative plots in Fig. 2(d)(*i*)-(*iv*) manifest the gradual increase of the Fermi crossing and more linear dispersion when close to the DP, in accordance with the predicted TDS feature of TDBB [Fig. 2(e)].

Next, we performed similar ARPES measurements but with *s*-polarized photons to identify topological surface states of $BaTi_2Sb_2O$. Figure 3(a) shows the intensity plot along $\bar{\Gamma}$-$\bar{M}$ with *s*-polarized photons. Figure 3(b)(*i*) and (*ii*) represent intensity maps on the $k_m - k_z$ plane with *s*-polarized photons taken at E_F and E_F - 0.4 eV, respectively. Our results demonstrate negligible k_z dispersions for TI band, suggesting that bulk states have been significantly suppressed and surface states from TI are dominating here. The slight k_z dependence of the bulk TDS bands suggests a

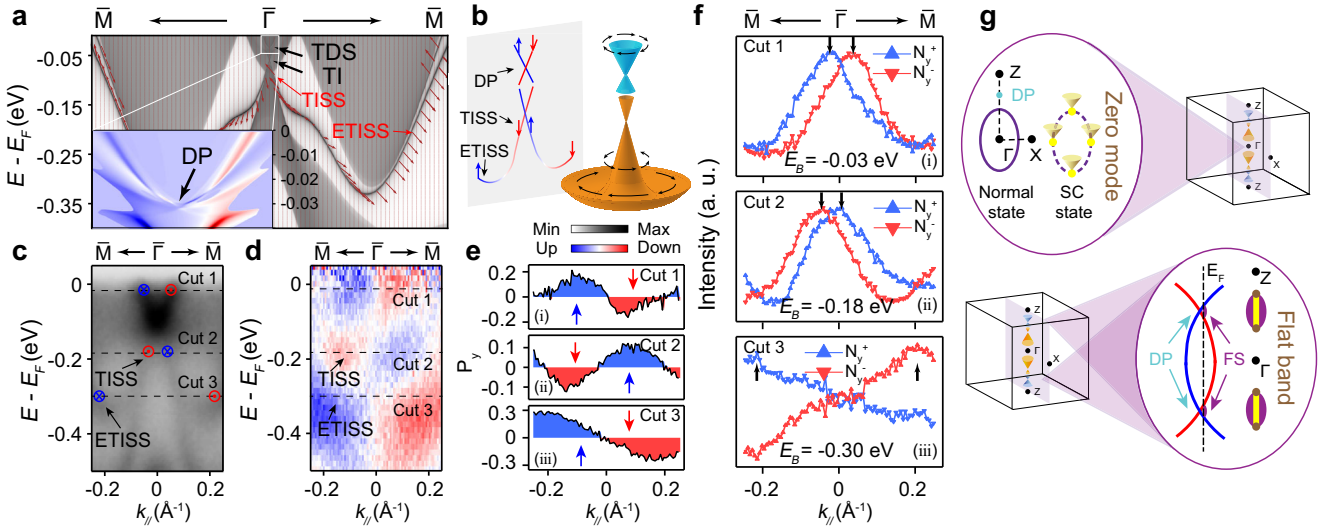

Fig. 4 Helical spin textures of surface states. a Calculated spin texture along $\bar{\Gamma}$-$\bar{M}$ direction. Inset: the enlarged image of the white box region. **b** Sketch of the spin-polarized characteristics of TDS and TI surface states. The red and blue lines express spin down and up, respectively. **c**, **d** Intensity plot measured without and with $\hat{y}$ direction spin-polarized along $\bar{\Gamma}$-$\bar{M}$ direction. The red and blue parts express spin direction along $-\hat{y}$ and $+\hat{y}$, respectively. **e** Spin polarization at Cut 1 to 3 in (**d**), indicating the spin texture of TDSS, TISS and ETISS. **f** Spin resolved MDCs taken at Cut 1 to 3. **g** Sketch of the dual topological superconductivity states induced by TDS states.

strong hybridization with TI surface states. Figure 3(c) displays the enlarged second derivative plot of band structure in the red box of Fig. 3(a). Together with the corresponding energy distribution curves (EDCs) [Fig. 3(d)], we can distinguish upper TDS cone and lower TI cone. The observed small gap could exclude the possibility of there being only one Dirac cone since no impurity scattering or symmetry breaking in $BaTi_2Sb_2O$. However, the lower TDS cone and upper TI cone in the gap are difficult for us to resolved. Furthermore, as exhibited by second derivative intensity plots in Fig. 3(e) and (f), detailed evolution of these surface cones along k_x and k_m could be recognized in evidence. The in-plane dispersion migrates apparently deviating Γ at different k_x and k_m positions, suggesting that both surface DPs are exactly located at $\bar{\Gamma}$.

Helical spin texture of the surface states

Both cones originating from TI and TDS should be spin-polarized, as suggested by our first-principles calculations [Fig. 4(a) and the inset]. States from the upper part of TDBB, the lower part (TISS) and extension of TI cone (ETISS) all suggest the same characteristic left-hand spin helicity as Li(Fe,Co)As and most TIs, which is then further confirmed by our constant-energy spin texture calculations shown in Supplementary Fig. S3 and Note 5. We then used spin-resolved ARPES to check these predictions. Here, for easy comparison, we summarized the sketch of spin nature of three surface states in Fig. 4(b) according to calculations. Figures 4(c) and (d) show our photoemission intensity plots without and with $\hat{y}$ direction spin-resolved measurement in the same region under more surface sensitive *s*-polarized photons, respectively. Evidently, for both TI and TDS cones, the left hand parts of these cones show the opposite spin direction to those of right hand parts, consistent with our calculations. Moreover, as displayed in Fig. 4(e), spin-resolved MDCs taken at $E_B = -0.03$ eV (Cut 1), -0.18 eV (Cut 2) and -0.30 eV (Cut 3) intersecting TDBB, TISS and ETISS demonstrate strong spin polarization up to 0.3. We note that the observed spin-polarized TDBB located in the energy range for the bulk Dirac bands, but is actually derived from the surface states of the bulk Dirac bands, since their unavoidably overlap on the (001) surface. Meanwhile, MDCs of partial intensities along $-\hat{y}$ and $+\hat{y}$ at Cut 1 to 3 in Fig. 4(f) also support the spin polarization result [see more details in Supplementary Fig. S4 and Note 6]. We note that these MDCs' peaks (marked as black arrows) indicate the exact momentum of surface bands, which are consistent with general ARPES results in Fig. 4(c).

DISCUSSION

The coexistence of spin-helical topological surface states and the bulk TDS in $BaTi_2Sb_2O$ resembles that of iron-based superconductor, such as Li(Fe,Co)As and Fe(Te,Se) [See details in Supplementary Note 7]. The DPs formed by the band inversion between Ti-*d* and Sb-*p* stay slightly below E_F, which naturally forms a FS with mixing parities - a necessary ingredient for the emergent TSC in TDS[77]. On the side surface, such as (010) schematically shown in Fig. 4(g), the bulk DPs map to different surface nodes and there may exist Fermi arcs/loops between the two DPs[79]. They would be gaped by superconducting order except for the nodes along Γ-*Z* and Γ-*X*, forming four zero energy Majorana modes. More interestingly, the parity-mixing Fermi surface above the DPs, as shown by the violet sphere in Fig. 4(g), would be gaped as well. However, as long as the surface admits the mirror symmetry along *y*-direction, Majorana flat-bands will appear as symmetry-protected TSC. Besides the promising topological superconductivity induced by the TDBB, the TISS extending to E_F and its hybridization with the bulk bands could also generate topological superconducting states similar to other iron-superconductors and TI-SC hybrid systems. Due to the proximity of the TDBB and TISS cone in $BaTi_2Sb_2O$, we cannot identify the dominant one. We actually believe both TDBB and TISS contribute to the topological superconductivity in this system. We note that our preliminary STM measurements on $BaTi_2Sb_2O$ have revealed its superconducting gap of 0.135 meV which mainly tends to come from the TDSS, and the upper branch of the TISS [see more details in Supplementary Figs. S5 to S7 and Note 8]. Compared to the DPs above the E_F in Fe(Te,Se), whose TSC has been confirmed after many optimizations and a long time of trying, the DPs of $BaTi_2Sb_2O$ is slightly below the E_F, which could dominate the low-energy electronic structure. Thus, $BaTi_2Sb_2O$, not belonging to any existing iron-based

superconductor family, provides another exciting platform for exploring the proximity effect in momentum space, which will greatly enrich the potential TSC family and offer independent insights for examining the current understanding of the TSC. Furthermore, compared to Li(Fe,Co)As, as no further electron doping is required in $BaTi_2Sb_2O$, the perfect alignment of E_F and DPs, namely, the DP is located slightly below E_F in $BaTi_2Sb_2O$, makes it the one of the most promising candidates to detect multiple-type TSC in one system. Besides, we note that the hole doping in $Ba_{1-x}Na_xTi_2Sb_2O$ will further enhance the superconductivity and increase the critical temperature to as high as 5.5 K while maintaining TI/TDS topology, see also Supplementary Fig. S8 and note 9[76,80].

In summary, we have identified the symmetry protected TDS, the TI states and their spin-momentum locking patterns in the titanium-based oxypnictide superconductor $BaTi_2Sb_2O$ by ARPES measurements in association with first-principles calculations. The helical surface states of the TDS slightly below E_F could naturally host both Majorana zero mode and flat band in this system. Therefore, $BaTi_2Sb_2O$ is an excellent platform for studying various types of Majorana fermions and for further research of topological superconductivity.

METHODS

Sample growth and characterizations

High-quality single crystals of $BaTi_2Sb_2O$ were grown by using $BaSb_2$ as the flux. Pieces of Ba (99.95%), Sb (99.999%) and TiO (99.9%) were mixed with an atomic ratio of Ba : Sb : TiO = 10 : 20 : 1, and then placed in an alumina crucible. This crucible was later sealed into a tantalum tube, which was then sealed into a quartz tube. The assembly was heated up to 1100 °C, maintained more than 30 hours, and was then slowly cooled down to 900 °C at a temperature decreasing rate of 2 °C/h. At 580 °C the flux was immediately separated in a high speed centrifuge. $BaTi_2Sb_2O$ single crystals were thus obtained in the aluminium oxide crucible.

ARPES experiments

High-resolution and spin-resolved ARPES measurements were performed at 03U and "Dreamline" beam lines of Shanghai Synchrotron Radiation Facility (SSRF), respectively. The 03U endstation is equipped with a Scienta Omicron DA30 electron analyzer. All ARPES data were taken at 15 K in an ultrahigh vacuum better than 8.0×10^{-11} Torr. The angular and the energy resolutions were set to 0.2° and 6 ~ 20 meV (dependent on the selected probing photon energy), respectively. The spin-resolved ARPES at "Dreamline" is equipped with a Scienta Omicron DA30-L electron analyzer together with a spin detector based on the very-low-energy-electron-diffraction (VLEED).

Band calculations

First-principles calculations were performed within the framework of the projector augmented wave (PAW) method and selected the generalized gradient approximation (GGA) with Perdew-Burke-Ernzerhof (PBE) type, as encoded in the Vienna Ab initio Simulation Package (VASP). A kinetic energy cutoff of 500 eV, a Γ-centred k mesh of $12 \times 12 \times 6$, and an energy difference criterion 10^{-6} eV were utilized for all calculations. The spin-orbit coupling (SOC) was considered in a self-consistent manner. The WANNIER90 package was adopted to construct Wannier functions from the first-principles results. Topological properties calculations were carried out with our in-house code *TMC*.

STM/S experiments

The STM/S measurements were carried out in a scanning tunneling microscope (USM-1300, Unisoku Co., Ltd.) with the lowest temperature of 0.4 K. The samples were cleaved in an ultra-high vacuum with a base pressure about 1×10^{-10} Torr. Pt/Ir tips were used after treatment on the Au(111) surface. The d*I*/d*V* spectra are collected using a standard lock-in technique with modulation frequency $f = 731$ Hz and typical modulation amplitude of 20-50 μV. The vortex images are measured by zero bias conductance mapping.

DATA AVAILABILITY

The authors declare that the main data supporting the findings of this study are available within the paper and its Supplementary Information files. Extra data are available from the corresponding authors upon request.

Received: 14 September 2021; Accepted: 9 June 2022;
Published online: 28 June 2022

REFERENCES

1. Hatsugai, Y. Chern number and edge states in the integer quantum Hall effect. *Phys. Rev. Lett.* **71**, 3697–3700 (1993).
2. Teo, J. C. & Kane, C. L. Topological defects and gapless modes in insulators and superconductors. *Phys. Rev. B* **82**, 115120 (2010).
3. Tanaka, Y., Sato, M. & Nagaosa, N. Symmetry and topology in superconductors–odd-frequency pairing and edge states–. *J. Phys. Soc.* **81**, 011013 (2011).
4. Alicea, J. New directions in the pursuit of Majorana fermions in solid state systems. *Rep. Prog. Phys.* **75**, 076501 (2012).
5. Aguado, R. Majorana quasiparticles in condensed matter. *Riv. del. Nuovo Cim.* **40**, 523–593 (2017).
6. Qi, X.-L. & Zhang, S.-C. Topological insulators and superconductors. *Rev. Mod. Phys.* **83**, 1057–1110 (2011).
7. Leijnse, M. & Flensberg, K. Introduction to topological superconductivity and Majorana fermions. *Semicond. Sci. Technol.* **27**, 124003 (2012).
8. Beenakker, C. Search for Majorana fermions in superconductors. *Annu. Rev. Condens. Matter Phys.* **4**, 113–136 (2013).
9. Stanescu, T. D. & Tewari, S. Majorana fermions in semiconductor nanowires: fundamentals, modeling, and experiment. *J. Phys. Condens. Matter* **25**, 233201 (2013).
10. Elliott, S. R. & Franz, M. Colloquium: Majorana fermions in nuclear, particle, and solid-state physics. *Rev. Mod. Phys.* **87**, 137–163 (2015).
11. Sarma, S. D., Freedman, M. & Nayak, C. Majorana zero modes and topological quantum computation. *NPJ Quantum Inf.* **1**, 15001 (2015).
12. Sato, M. & Fujimoto, S. Majorana fermions and topology in superconductors. *J. Phys. Soc. Jpn.* **85**, 072001 (2016).
13. Sato, M. & Ando, Y. Topological superconductors: a review. *Rep. Prog. Phys.* **80**, 076501 (2017).
14. Read, N. & Green, D. Paired states of fermions in two dimensions with breaking of parity and time-reversal symmetries and the fractional quantum Hall effect. *Phys. Rev. B* **61**, 10267–10297 (2000).
15. Kitaev, A. Y. Fault-tolerant quantum computation by anyons. *Ann. Phys. (N. Y)* **303**, 2–30 (2003).
16. Nayak, C., Simon, S. H., Stern, A., Freedman, M. & Sarma, S. D. Non-Abelian anyons and topological quantum computation. *Rev. Mod. Phys.* **80**, 1083–1159 (2008).
17. Mackenzie, A. P. & Maeno, Y. The superconductivity of Sr_2RuO_4 and the physics of spin-triplet pairing. *Rev. Mod. Phys.* **75**, 657–712 (2003).
18. Fu, L. & Berg, E. Odd-parity topological superconductors: theory and application to $Cu_xBi_2Se_3$. *Phys. Rev. Lett.* **105**, 097001 (2010).
19. Sato, M. Topological odd-parity superconductors. *Phys. Rev. B* **81**, 220504 (2010).
20. Hsieh, T. H. & Fu, L. Majorana fermions and exotic surface andreev bound states in topological superconductors: application to $Cu_xBi_2Se_3$. *Phys. Rev. Lett.* **108**, 107005 (2012).
21. Fu, L. & Kane, C. L. Superconducting proximity effect and Majorana fermions at the surface of a topological insulator. *Phys. Rev. Lett.* **100**, 096407 (2008).
22. Qi, X.-L., Hughes, T. L. & Zhang, S.-C. Topological invariants for the Fermi surface of a time-reversal-invariant superconductor. *Phys. Rev. B* **81**, 134508 (2010).
23. Lutchyn, R. M. et al. Majorana zero modes in superconductor–semiconductor heterostructures. *Nat. Rev. Mater.* **3**, 52–68 (2018).
24. Frolov, S., Manfra, M. & Sau, J. Topological superconductivity in hybrid devices. *Nat. Phys.* **16**, 718–724 (2020).
25. Alicea, J. Majorana fermions in a tunable semiconductor device. *Phys. Rev. B* **81**, 125318 (2010).
26. Sau, J. D., Lutchyn, R. M., Tewari, S. & Sarma, S. D. Generic new platform for topological quantum computation using semiconductor heterostructures. *Phys. Rev. Lett.* **104**, 040502 (2010).
27. Lutchyn, R. M., Sau, J. D. & Sarma, S. D. Majorana fermions and a topological phase transition in semiconductor-superconductor heterostructures. *Phys. Rev. Lett.* **105**, 077001 (2010).
28. Oreg, Y., Refael, G. & Von Oppen, F. Helical liquids and Majorana bound states in quantum wires. *Phys. Rev. Lett.* **105**, 177002 (2010).

29. Chung, S. B., Zhang, H.-J., Qi, X.-L. & Zhang, S.-C. Topological superconducting phase and Majorana fermions in half-metal/superconductor heterostructures. *Phys. Rev. B* **84**, 060510 (2011).
30. Duckheim, M. & Brouwer, P. W. Andreev reflection from noncentrosymmetric superconductors and Majorana bound-state generation in half-metallic ferromagnets. *Phys. Rev. B* **83**, 054513 (2011).
31. Kashiwaya, S. et al. Edge states of Sr_2RuO_4 detected by in-plane tunneling spectroscopy. *Phys. Rev. Lett.* **107**, 077003 (2011).
32. Jang, J. et al. Observation of half-height magnetization steps in Sr_2RuO_4. *Science* **331**, 186–188 (2011).
33. Hor, Y. S. et al. Superconductivity in $Cu_xBi_2Se_3$ and its implications for pairing in the undoped topological insulator. *Phys. Rev. Lett.* **104**, 057001 (2010).
34. Wray, L. A. et al. Observation of topological order in a superconducting doped topological insulator. *Nat. Phys.* **6**, 855–859 (2010).
35. Sasaki, S. et al. Topological superconductivity in $Cu_xBi_2Se_3$. *Phys. Rev. Lett.* **107**, 217001 (2011).
36. Matano, K., Kriener, M., Segawa, K., Ando, Y. & Zheng, G.-q Spin-rotation symmetry breaking in the superconducting state of $Cu_xBi_2Se_3$. *Nat. Phys.* **12**, 852–854 (2016).
37. Yonezawa, S. et al. Thermodynamic evidence for nematic superconductivity in $Cu_xBi_2Se_3$. *Nat. Phys.* **13**, 123–126 (2017).
38. Liu, Z. et al. Superconductivity with topological surface state in $Sr_xBi_2Se_3$. *J. Am. Chem. Soc.* **137**, 10512–10515 (2015).
39. Tanaka, Y. et al. Two types of Dirac-cone surface states on the (111) surface of the topological crystalline insulator SnTe. *Phys. Rev. B* **88**, 235126 (2013).
40. Williams, J. et al. Unconventional Josephson effect in hybrid superconductor-topological insulator devices. *Phys. Rev. Lett.* **109**, 056803 (2012).
41. Wang, M.-X. et al. The coexistence of superconductivity and topological order in the Bi_2Se_3 thin films. *Science* **336**, 52–55 (2012).
42. Wang, E. et al. Fully gapped topological surface states in Bi_2Se_3 films induced by a d-wave high-temperature superconductor. *Nat. Phys.* **9**, 621–625 (2013).
43. Cho, S. et al. Symmetry protected Josephson supercurrents in three-dimensional topological insulators. *Nat. Commun.* **4**, 1689 (2013).
44. Oostinga, J. B. et al. Josephson supercurrent through the topological surface states of strained bulk HgTe. *Phys. Rev. X* **3**, 021007 (2013).
45. Finck, A., Kurter, C., Hor, Y. S. & Van Harlingen, D. J. Phase coherence and Andreev reflection in topological insulator devices. *Phys. Rev. X* **4**, 041022 (2014).
46. Hart, S. et al. Induced superconductivity in the quantum spin Hall edge. *Nat. Phys.* **10**, 638–643 (2014).
47. Mourik, V. et al. Signatures of Majorana fermions in hybrid superconductor-semiconductor nanowire devices. *Science* **336**, 1003–1007 (2012).
48. Rokhinson, L. P., Liu, X. & Furdyna, J. K. The fractional ac Josephson effect in a semiconductor–superconductor nanowire as a signature of Majorana particles. *Nat. Phys.* **8**, 795–799 (2012).
49. Das, A. et al. Zero-bias peaks and splitting in an Al–InAs nanowire topological superconductor as a signature of Majorana fermions. *Nat. Phys.* **8**, 887–895 (2012).
50. Deng, M. et al. Anomalous zero-bias conductance peak in a Nb–InSb nanowire–Nb hybrid device. *Nano Lett.* **12**, 6414–6419 (2012).
51. Churchill, H. et al. Superconductor-nanowire devices from tunneling to the multichannel regime: Zero-bias oscillations and magnetoconductance crossover. *Phys. Rev. B* **87**, 241401 (2013).
52. Finck, A., Van Harlingen, D., Mohseni, P., Jung, K. & Li, X. Anomalous modulation of a zero-bias peak in a hybrid nanowire-superconductor device. *Phys. Rev. Lett.* **110**, 126406 (2013).
53. Lee, E. J. et al. Spin-resolved Andreev levels and parity crossings in hybrid superconductor–semiconductor nanostructures. *Nat. Nanotechnol.* **9**, 79–84 (2014).
54. Nadj-Perge, S. et al. Observation of Majorana fermions in ferromagnetic atomic chains on a superconductor. *Science* **346**, 602–607 (2014).
55. Albrecht, S. M. et al. Exponential protection of zero modes in Majorana islands. *Nature* **531**, 206–209 (2016).
56. Deng, M. et al. Majorana bound state in a coupled quantum-dot hybrid-nanowire system. *Science* **354**, 1557–1562 (2016).
57. Chen, J. et al. Experimental phase diagram of zero-bias conductance peaks in superconductor/semiconductor nanowire devices. *Sci. Adv.* **3**, e1701476 (2017).
58. Suominen, H. J. et al. Zero-energy modes from coalescing Andreev states in a two-dimensional semiconductor-superconductor hybrid platform. *Phys. Rev. Lett.* **119**, 176805 (2017).
59. Nichele, F. et al. Scaling of Majorana zero-bias conductance peaks. *Phys. Rev. Lett.* **119**, 136803 (2017).
60. Zhang, H. et al. Ballistic superconductivity in semiconductor nanowires. *Nat. Commun.* **8**, 16025 (2017).
61. Zhang, H. et al. Quantized Majorana conductance. *Nature* **556**, 74–79 (2018).
62. Kim, H. et al. Toward tailoring Majorana bound states in artificially constructed magnetic atom chains on elemental superconductors. *Sci. Adv.* **4**, eaar5251 (2018).
63. Kezilebieke, S. et al. Topological superconductivity in a van der Waals heterostructure. *Nature* **588**, 424–428 (2020).
64. Zhang, T. et al. Observation of distinct spatial distributions of the zero and nonzero energy vortex modes in $(Li_{0.84}Fe_{0.16})$OHFeSe. *Phys. Rev. Lett.* **126**, 127001 (2021).
65. Zhang, P. et al. Observation of topological superconductivity on the surface of an iron-based superconductor. *Science* **360**, 182–186 (2018).
66. Wang, D. et al. Evidence for Majorana bound states in an iron-based superconductor. *Science* **362**, 333–335 (2018).
67. Gray, M. J. et al. Evidence for helical hinge zero modes in an Fe-based superconductor. *Nano Lett.* **19**, 4890–4896 (2019).
68. Machida, T. et al. Zero-energy vortex bound state in the superconducting topological surface state of Fe (Se, Te). *Nat. Mater.* **1**, 811–815 (2019).
69. Kong, L. et al. Half-integer level shift of vortex bound states in an iron-based superconductor. *Nat. Phys.* **15**, 1181–1187 (2019).
70. Wang, Z. et al. Evidence for dispersing 1D majorana channels in an iron-based superconductor. *Science* **367**, 104–108 (2020).
71. Zhu, S. et al. Nearly quantized conductance plateau of vortex zero mode in an iron-based superconductor. *Science* **367**, 189–192 (2020).
72. Zhang, P. et al. Multiple topological states in iron-based superconductors. *Nat. Phys.* **15**, 41–47 (2019).
73. Aswartham, S. et al. Suppressed superconductivity in charge-doped $Li(Fe_{1-x}Co_x)As$ single crystals. *Phys. Rev. B* **84**, 054534 (2011).
74. Pitcher, M. J. et al. Compositional control of the superconducting properties of LiFeAs. *J. Am. Chem. Soc.* **132**, 10467–10476 (2010).
75. Yajima, T. et al. Superconductivity in $BaTi_2Sb_2O$ with a d^1 square lattice. *J. Phys. Soc.* **81**, 103706 (2012).
76. Song, Q. et al. Electronic structure of the titanium-based oxypnictide superconductor $Ba_{0.95}Na_{0.05}Ti_2Sb_2O$ and direct observation of its charge density wave order. *Phys. Rev. B* **93**, 024508 (2016).
77. Kawakami, T. & Sato, M. Topological crystalline superconductivity in Dirac semimetal phase of iron-based superconductors. *Phys. Rev. B* **100**, 094520 (2019).
78. Damascelli, A., Hussain, Z. & Shen, Z.-X. Angle-resolved photoemission studies of the cuprate superconductors. *Rev. Mod. Phys.* **75**, 473 (2003).
79. Yang, B.-J. & Nagaosa, N. Classification of stable three-dimensional Dirac semimetals with nontrivial topology. *Nat. Commun.* **5**, 4898 (2014).
80. Doan, P. et al. $Ba_{1-x}Na_xTi_2Sb_2O$ ($0.0 \le x \le 0.33$): A layered titanium-based pnictide oxide superconductor. *J. Am. Chem. Soc.* **134**, 16520–16523 (2012).

ACKNOWLEDGEMENTS

This work is supported by the NSFC (Grant Nos. U2032208, 92065201, 11874263, 12004405), the National Key R&D Program of the MOST of China (Grants Nos. 2017YFE0131300 and 2016YFA0401002), the Strategic Priority Research Program of CAS (Grant No. XDA18010000) and the Natural Science Foundation of Shanghai (Grant No. 14ZR1447600) and Shanghai Technology Innovation Action Plan (2020-Integrated Circuit Technology Support Program 20DZ1100605, 2021-Fundamental Research Area 21JC1404700), and Sino-German Mobility program (M-0006). Y.F.G. and G.L. acknowledge the starting grant of ShanghaiTech University and the Program for Professor of Special Appointment (Shanghai Eastern Scholar). Y.B.H. acknowledges the CAS Pioneer "Hundred Talents Program" (type C). D.W.S. is supported by "Award for Outstanding Member in Youth Innovation Promotion Association CAS". J.S.L. thanks the fund of Science and Technology on Surface Physics and Chemistry Laboratory (6142A02200102). Part of this research used Beamline 03U of the Shanghai Synchrotron Radiation Facility, which is supported by ME2 project under contract No. 11227902 from National Natural Science Foundation of China. Calculations were carried out at the HPC Platform of ShanghaiTech University Library and Information Services, and at School of Physical Science and Technology. The authors also thank the support from the Analytical Instrumentation Center (SPST-AIC10112914), SPST, ShanghaiTech University.

AUTHOR CONTRIBUTIONS

D.W.S. conceived this research project; Y.F.G., L.G. and D.W.S. designed the research; W.L.L. and Z.H. performed ARPES measurement; S.Y.G. and Z.H. performed spin-resolved ARPES measurement; Z.Y.C. and Y.J.Y. performed STM measurement; Y.L.S. and G.L. carried out theoretical calculations; H.Y.W. and Y.F.G. synthesized the single crystals. Z.H., G.L., and D.W.S. wrote the manuscript with input from all authors.

COMPETING INTERESTS

The authors declare no competing interests.

ADDITIONAL INFORMATION

Supplementary information The online version contains supplementary material available at https://doi.org/10.1038/s41535-022-00477-z.

Correspondence and requests for materials should be addressed to Y. F. Guo, G. Li or D. W. Shen.

Reprints and permission information is available at http://www.nature.com/reprints

Publisher's note Springer Nature remains neutral with regard to jurisdictional claims in published maps and institutional affiliations.